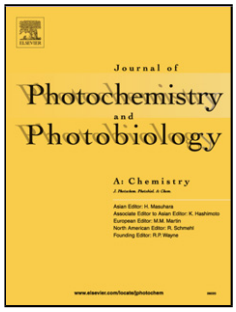

Title: Insight into the fluorescence quenching of Trp214 at HSA by the Dimetridazole ligand from simulation

Authors: Vladimir A. Pomogaev, Ruslan R. Ramazanov, Kenneth Ruud, Victor Ya. Artyukhov

PII: S1010-6030(17)30092-8
DOI: http://dx.doi.org/10.1016/j.jphotochem.2017.08.041
Reference: JPC 10816

To appear in: *Journal of Photochemistry and Photobiology A: Chemistry*

Received date: 31-1-2017
Revised date: 17-8-2017
Accepted date: 17-8-2017

Please cite this article as: Vladimir A.Pomogaev, Ruslan R.Ramazanov, Kenneth Ruud, Victor Ya.Artyukhov, Insight into the fluorescence quenching of Trp214 at HSA by the Dimetridazole ligand from simulation, Journal of Photochemistry and Photobiology A: Chemistryhttp://dx.doi.org/10.1016/j.jphotochem.2017.08.041

Insight into the fluorescence quenching of Trp214 at HSA by the Dimetridazole ligand from simulation.

Vladimir A. Pomogaev[1*], Ruslan R. Ramazanov[2], Kenneth Ruud[3], Victor Ya. Artyukhov[1]

[1]*Tomsk State University, 36 Lenin Avenue, Tomsk, Russia*
[2]*Department of Molecular Biophysics and Polymer Physics, V.A. Fock Institute of Physics St. Petersburg State University, 1 Ulianovskaya Str., Petrodvorets, St. Petersburg, Russia*
[3]*Centre for Theoretical and Computational Chemistry, Department of Chemistry, University of Tromsø – The Arctic University of Norway, N-9037 Tromsø, Norway.*

Graphical abstract

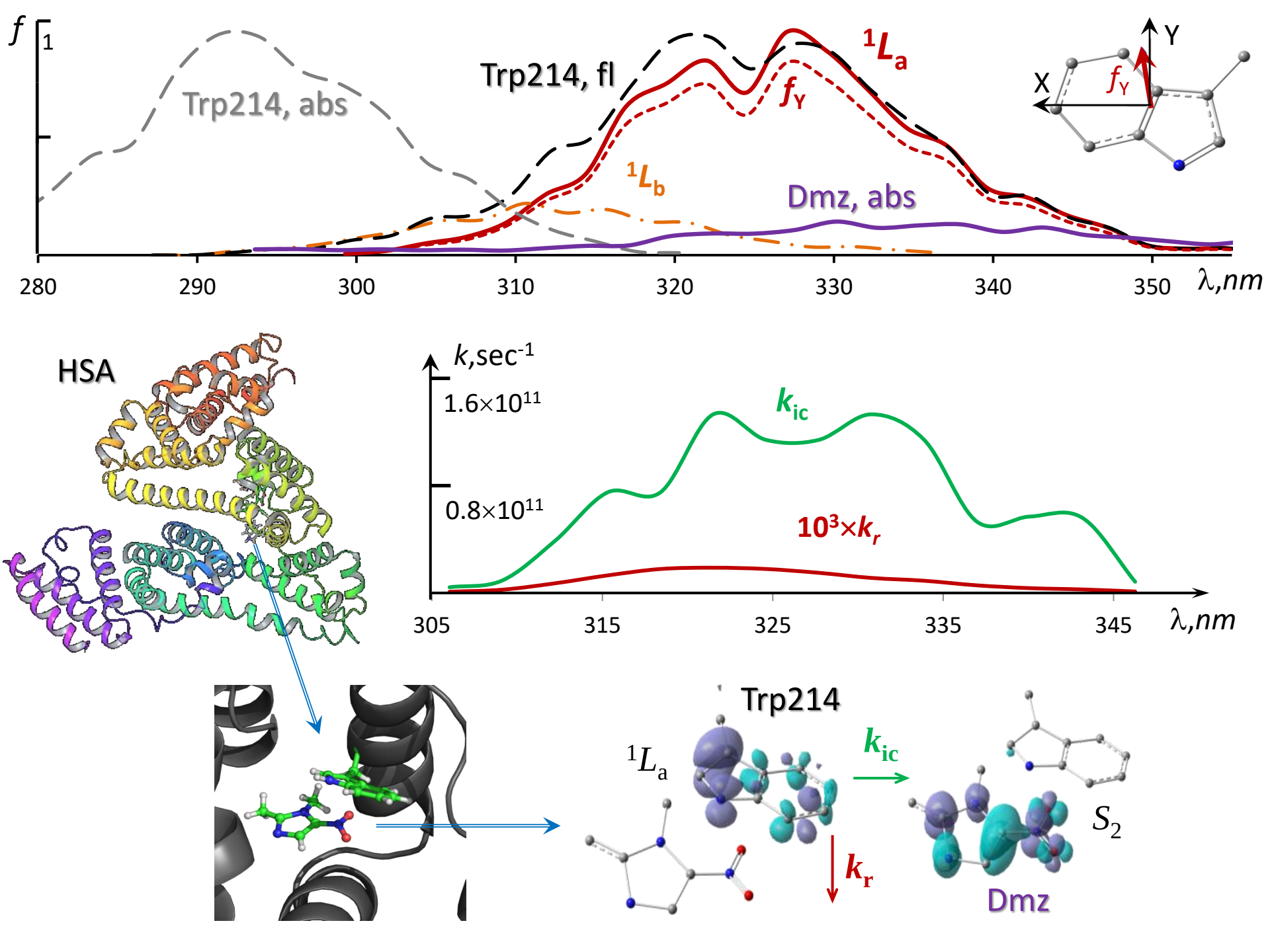
f
1
Trp214, abs
Trp214, fl
^1L_a
f_Y
^1L_b
Dmz, abs
Y
X
f_Y
280
290
300
310
320
330
340
350
λ,nm
HSA
k,sec^{-1}
1.6×10^{11}
0.8×10^{11}
k_{ic}
10^3×k_r
305
315
325
335
345
λ,nm
Trp214
^1L_a
k_{ic}
k_r
S_2
Dmz

Highlights

Absorption, emission, and fluorescence quenching in various conformers of the dimetridazole and tryptophan residue complex in the binding cavity of Human Serum Albumin (Dmz&Trp214@HSA) were calculated with implementing the two-scale model of MD simulation and various quantum-mechanical approaches in order to generate statistical spectra that are then used for studying the charge transfer processes between the non-bonded Trp214 donor and the Dmz acceptor where types of these intermolecular processes were identified.

Spectroscopy is an important tool for detecting drug binding to amino acid sequences. One such important spectroscopic process is the fluorescence quenching due to charge transfer (CT) processes between a drug molecule and the chromophore centre of Human Serum Albumin (HSA). We present a theoretical investigation of the CT occurring upon electronic excitation when a dimetridazole (Dmz) molecule incorporated in HSA interacts with tryptophan residue (Trp214). Structures of the donor–acceptor complexes were optimized using density-functional theory in vacuum as well as extracted from molecular dynamics (MD) trajectories of the Dmz and Trp214 complexes in HSA (Dmz&Trp214@HSA). Absorption, emission, and fluorescence quenching of the Trp214&Dmz complex in a large number of MD conformers were calculated using various quantum-mechanical approaches in order to generate statistical spectra that are then used for studying the CT between the non-bonded donor and the acceptor.

Keywords: Human Serum Albumin; tryptophan residue; dimetridazole acceptor; molecular dynamics; quantum-mechanics; charge transfer.

Introduction

Spectroscopic methods used in medicine and pharmacology can provide valuable insight into the electronic and structural properties of biological polymers based on their photo-physical and photo-chemical reactions [1]. Spectroscopy can also be used to monitor, control, test, and develop protein chains and drug compounds [2–6]. Chemical and morphological properties of amino acid sequences can be investigated in situ using luminescent (fluorescent or phosphorescent) markers or using molecular probes possessing easily identifiable spectral signatures [7,8]. Theoretical methods have been used to interpret and unravel the complicated structural and electronic origins of experimental spectra [9–11]. A perfect benchmark for verifying, developing, and applying theoretical methods in the investigation of spectral properties is the tryptophan aromatic amino acid (Fig. 1) that is contained in numerous biological chains.

The tunable fluorescence maxima and intensity of tryptophan (2-Amino-3-(1*H*-indol-3-yl)propanoic acid) is widely used as a probe of the electrostatic microenvironment produced by surrounding solvents and proteins. Absorption in the near- and far-ultraviolet regions (220-190 nm) of protein spectra arises from the aromatic amino acids phenylalanine (Phe), tyrosine (Tyr), the highly intense L_b bands of tryptophan (Trp), and histidine (His) residues and coincides with the absorption region of peptide or the amide chromophores [1,12–15]. Tyr and the less intense L_a bands of Trp mainly contribute to the spectral region between 240-280 nm [16,17]. In contrast, the fluorescence maximum is due only to UV-excited Trp [18–20], but varies between 307 and 370 nm and in some cases even longer wavelengths depending on the microenvironment. In particular, the single Trp214 chromophore side residue is solely responsible for the long-wavelength wing of the HSA (Trp214@HSA) spectrum starting from 300 nm (Figures 2 and 3) [19,21].

It is well established that the chromophore core of tryptophan is the methyl-terminated form of 3-methylindole fragment, also known as skatole [2,3,22,23]. At room temperature, the

maximum of the fluorescence spectrum is located near λ = 308-310 nm in non-polar solvents and significantly shifted towards longer wavelengths in more polar solvents, reaching a fluorescence wavelength of 340-350 nm in water, consistent with the observed fluorescence from Trp214 in HSA.

The single Trp214 residue in HSA is located within a hydrophobic binding pocket of the molecule [24,25] in subdomain IIA of drug site I, where most potential drug molecules can be bonded. This fact, combined with the very characteristic absorption and fluorescence properties of the Trp214 residue, allow for detecting whether drug molecules are bonded to HSA and to follow their transport with the blood flow. A bio-ligand trapped at the drug site near Trp214 can thus be considered a photochemical probe of the complexation state of HSA if it induces fluorescence quenching due to charge transfer (CT) between the Trp214 donor and the ligand acceptor of this complex.

It has been reported that a dimetridazole (Dmz; $C_5H_7N_3O_2$, 1,2-dimethyl-5-nitroimidazole) embedded in this pocket leads to a quenching of the strong HSA fluorescence in the wavelength region λ_{em}=342−345 nm (Fig. 3) due to excited-state energy transfer from the chromophore center to Dmz [19]. This complex can thus serve as a model system for studying the CT between spatially close, non-bonded fragments of a complex trapped in the tight space of HSA.

We will here investigate the mechanism for redistributing the excitation energy and the transfer of charge from Trp214 to the Dmz ligand trapped in the same subdomain of HSA using MD simulation and quantum-mechanical (QM) calculations. This will allow us to understand how the separation and relative orientation of the donor and the ligand acceptor influence the spectral shifts and the excited-state energy deactivation through fluorescence quenching of the fluorescence spectrum of this complex.

The rest of the paper is organized as follows. In the next section, we will summarize our computational approach, before we in Section 2 discuss our results, both for the isolated chromophore and for the chromophore embedded in the protein structure and interacting with the ligand. In the last section, we give some concluding remarks and an outlook.

1 Computational methods

We will in Section 1.1 describe the approach used for the QM optimization of the chromophore centers in the ground and excited states; the computational details of the MD simulations are described in Section 1.2; and the Statistical Quantum-Mechanical/Molecular-Dynamics (SQMMD) method for generating the optical spectra is described in Section 1.3.

1.1 Geometry optimization and Spectral properties

Indole and 3-methylindole (skatole) were used to calculate excitation and emission spectra. The ground and the two lowest excited states of these molecules as well as Dmz were optimized separately in vacuum using time-dependent DFT (TDDFT) in Gaussian 09 (G09) [26]. This was done using the aug-cc-pVDZ basis set [27] and the hybrid, long-range (LC) corrected CAM-B3LYP functional [28] (CMB/aug). The CAM-B3LYP functional has been shown to perform well for CT excitations [29,30]. These optimized structures were also used to calculate the excited states and the transfer of charge between the non-bonded donor and the acceptor. In addition, the sequence of three amino acids Ala213–Trp214–Ala215 of HSA and tryptophan itself were constructed starting from the ground- and excited-state optimized indole core structures calculated with CMB/aug (*vide infra*).

TDDFT vertical excitation energies were calculated for skatole in vacuum using CMB/aug in Dalton2013.4 [31,32] and G09. Several calculations using CAM-B3LYP and the PBE0 exchange–correlation functional [33] in combination with various basis sets such as SVP, 6-311++g(d,p) and def2TZVP were carried out to estimate the sensitivity of the TDDFT results on basis set and choice of exchange-correlation functional. However, all basis sets and functionals gave very similar results, showing deviations of about 3 nm for the lowest states. Equation-of-

motion coupled cluster with single- and double-excitations (EOM-CCSD) with the aug-cc-pVDZ basis set were also calculated for a few of the smallest systems to assess the quality of the DFT results.

The spectroscopically oriented semi-empirical Intermediate Neglect of Differential Overlap (INDO) method in a sp-basis (INDO/sp), which is similar to the ZINDO method and successfully applied by Callis and coauthors in numerous works for decades [3,34,35], has been adjusted to provide correct transition energies to Franck-Condon states by calibrating multi-center Coulomb and exchange integrals to spectroscopic data for organic compounds. This has been implemented in a standalone code and in a development version of GAMESS-09 [36] as the Quantum Chemistry of Organic Photonics (QOP) blocks [10,22,36]. The parameters were calibrated against experimental data for representative molecules in the ground state geometry in a non-polar aprotic solvent at low temperature, as previously described in Ref. [37]. QOP has options for calculating the rates of radiative, internal conversion [38,39] and intersystem crossing (cross-section) transition [40,41], allowing the quantum yields of photoprocesses to be estimated. The probability of internal conversion between non-bonded parts in a super-molecule can be used to estimate the rate of CT between these two fragments. Excited states are calculated using a Configuration Iteration Singles (CIS) approach in which the number of MOs involved in the electronic configurations can be selected. In order to use the same MOs in the isolated molecules and in the corresponding bimolecular complex, the following CIS settings were applied: 20 highest occupied MOs and the 25 lowest unoccupied MOs (20×25 for skatole (Skt) and Dmz, 40×45 for their Skt&Dmz complex).

1.2 System preparation and MD simulation

The 1H9Z crystal structure of HSA [42] was obtained from the Protein Data Bank [43] and preprocessed using GROMACS [44] to prepare an initial structure of 1H9Z, which originally contains the warfarin ligand in subdomain IIA of drug site I, 28 crystal water molecules and 6 unsaturated myristic fatty acids in addition to the HSA protein [42].

The protein structures were solvated in an orthorhombic box filled with a NaCl buffer with distances of 10 Å between the protein atoms and the edges of the box. The TIP3P approach [45] was used to model the water molecules. Force field parameterization of skatole and DMZ molecules was performed on the basis of the OPLS-AA force field by use of the Tppmktop software [46] and calculated ESP partial charges (Table 2,3). GROMACS was used with slightly modified idealized stretching and bending OPLS-AA force field parameters for the indole ring. These optimal distances and angles were calibrated against the optimized structures of the ground- and excited-states of this fragment in order to produce reliable spectra of the indole chromophore in both the excited and the ground electronic states (see Table 2 and the discussion in Section 2.1).

1 ns of initial equilibration was performed in an NVT ensemble by gradually heating to 300 K with integration steps of 1 fs and all covalent bonds constrained by the LINear Constraint Solver (LINCS) algorithm [47]. After this step, a 5 ns MD trajectory with a Nose-Hoover thermostat (300 K), NPT ensemble and integration step of 2 fs, was run and sampled for representative structures. Hydrogen-heavy atom covalent bond lengths were constrained using the LINCS algorithm. Electrostatic interactions were computed using the Particle Mesh Ewald (PME) method with a Fourier spacing of 0.12. All calculations were done employing periodic boundary conditions.

As classical point charges cannot be unambiguously defined based on QM principles, there are a number of methods in use for representing a quantum-mechanical electron density in terms of classical point charges, such as the Mulliken, Hirshfeld, or Natural Bond Orbital population analysis [44–46].

The electrostatic potential (ESP) method implemented in G09 is based on calculated potentials in all points of space using a charged probe [51], and is used here as it can be expected to represent the relevant electrostatic interactions in the Dmz and Trp@HSA complexes. All the different indole fragments produce very similar point charges, allowing us to use the same set of averaged charges on the atoms for all the different structures, and these charges are listed in Tables 2 and 3. The use of averaged embedding potentials was also recently proposed as a cost-effective approach to multiscale modeling of molecular

properties [52]. These calculated point charges were kept fixed during the MD simulations because the total molecular charge distribution dominates the interaction with other surrounding particles at the VdW distances important for the complexes rather than any minor charge changes on the individual atoms. It has for instance been shown that feeding the QM-calculated point charges back to the MD simulation only lead to minor improvements in the description of the interaction of the indole chromophore with the microenvironment [53].

Optimized and standard OPLS-AA structures and charges for the DMZ ligand provide similar energies for the lowest excited states acting as acceptor states for the CT from the fluorescent state of the tryptophan donor. For this reason, only the optimized Dmz ground-state structure was used in the MD simulations.

1.3 Generating statistical optical spectra

The Statistical Quantum-Mechanical/Molecular-Dynamic (SQMMD) [10] technique was used to generate vibronic (electronic-vibrational) absorption spectra. In this approach, stereochemical structures, transition energies, and photophysical properties of each conformer extracted from a fluctuating molecular fragment along a MD trajectory are extracted and calculated at each time-step Δt. The effective spectral width is defined by the highest and lowest transition energies and divided into wavelength bins $\Delta\lambda$ that is determined by the instrumental and experimental conditions. When modeling, this interval should be in the range 0.5–4.0 nm and is estimated from the number of MD snapshots, N, the effective spectral width, and also the lifetime of the excited states of distorted molecular structures [10]. In a 5 ns MD simulation, the spectra would have $\Delta\lambda$ ~2.5 nm if the spectral properties of all N = 1000 conformers are used in the calculation.

An averaged band absorption intensity on a given $\Delta\lambda$ bin corresponds to the relative absorptivity $\varepsilon_{\Delta\lambda} = p_{\Delta\lambda} \cdot f_{\Delta\lambda,}$ where $p_{\Delta\lambda} = N_{\Delta\lambda}/N$ is the probability of finding the fluctuating molecule in an excited state in this energy interval, and the averaged oscillator strength $f_{\Delta\lambda}$ is defined by the oscillator strength of the $N_{\Delta\lambda}$ conformers in this $\Delta\lambda$ interval [10,22,36]. The relative emission intensity is estimated as the product of probabilities $I_{\Delta\lambda} = p_{\Delta\lambda} \cdot k_r \cdot \gamma_{\Delta\lambda}$ [10] where $\gamma = k_r/(k_r+\Sigma k_{st})$ is the quantum yield. The rate of fluorescence is defined by the oscillator strength and energy gap between the excited and ground states of the same multiplicity, using the formula $k_r = 2^{-1/2} f \cdot (E_{Sn} - E_{So})^2$ where the energy is given in cm^{-1}. The rate of internal conversion k_{ic} is determined in an approximate manner by only including C-H vibrations for organic compounds [10,38,39,54]. The rate of cross-section transition k_{st} is omitted in this work because this process is much less important than internal conversion for the system studied here, as will be shown later. If the intensity is normalized [55,56], the probability distribution is not needed. The statistical spectrum is obtained as an envelope over the intensities.

2. Results and discussion

The selection of a representative model for the chromophore in HSA able to correctly describe the lowest excited singlet states of the observed absorption profile will be discussed in Section 2.1. Tryptophan (Trp), 3-alanyl-indole (Trp without the OH group), Trp214 together with the two neighboring alanine Ala213 and Ala215 amino acids (Trp2Ala) as they are present in HSA, skatole, and the indole unit itself will be considered. The excited states, intensities, and dipole transition moments obtained using different QM methods in vacuum are discussed in subsection 2.1.1 for the ground-state structures and absorption properties, and in subsection 2.1.2 for the excited-state structures.

The MD trajectories of HSA obtained with two different OPLS-AA force fields scaled to reproduce absorption and emission spectra, respectively, of the indole chromophore were calculated and are discussed in subsection 2.2.1, together with the procedure for extracting snapshots of the complexes of skatole with Dmz (Skt&Dmz) along the MD trajectory. Subsection 2.2.2 focusses on a structural analysis of the selected donor-acceptor complexes in order to estimate the electronic coupling between them, as this will affect their potential for supporting charge-transfer excitations. Finally, in subsection 2.2.3, we present the SQMMD absorption and fluorescence spectra of skatole as well as the overlap of the skatole fluorescence and absorption bands with those of the Dmz ligands. Throughout the discussion, we will compare our results to available experimental data.

2.1 Isolated chromophore

2.1.1 Absorption structures

In order to reproduce spectral features of amino acid sequences that contain a tryptophan residue, an adequate chromophore model and computational methods capable of correctly calculating the energies of the excited states and their photo-physical properties are needed. A particular challenge is the presence of two overlapping and relatively weakly absorbing $\pi\pi^*$ transitions to the low-lying excited singlet states of the tryptophan residue, conventionally denoted as ^1L_b and ^1L_a. The wavelength of these absorption bands display a strong dependence on the environment, giving rise to a complex profile for the long-wavelength absorption band (240–300 nm) [2,57]. The key photophysical problem when studying indole-based compounds is to correctly detect, identify and separate these weak and close-lying ^1L_b and ^1L_a absorption bands by determining their oscillator strengths f_i and the orientations of the transition dipole moments μ_i. From a computational point of view, it is also important to describe the MOs involved in these excitation processes and their spatial structure. We will use electron density difference (EDD) maps between the electronic excited and ground states to obtain this insight.

To determine the smallest chromophore center capable of describing the relevant spectral properties of these absorption bands, five different models were prepared based on the indole topology, taken from Refs. [16,17]. Trp2Ala (Fig. 4), tryptophan (Fig. 1), 3-alanyl-indole, skatole (Fig. 5a) and indole (Fig. 5b) all give very similar results at the CMB/aug level of theory (Table 1). However, a reversal of the ordering of the two levels can be observed when the hydrogen is substituted by a methyl group or larger substituents at the 3-position of the C_γ atom. This is due to the fact that only the ^1L_a state involves MOs on the substituent, leading to a shift in the ^1L_a energy level and an overall reversal of the ordering of the ^1L_a and ^1L_b states (see Fig. 5). In Fig. 5 and in the rest of the paper, EDD isodensity surfaces are plotted using a threshold of 0.004 e^-/bohr^3 unless otherwise noted. As noted previously [17], the dipole moment of the^1L_a state and the interaction of this state with polar solvents are enhanced by internal CT between the conjugated five-membered pyrrole and six-membered benzene rings, whereas ^1L_b arises mainly from electron redistribution within the benzene unit. The shift in the electron density (ED) from the pyrrole ring to the benzene ring upon excitation to the ^1L_a state is very sensitive to the environment due to the involvement of the polar nitrogen atom in this transition, as have been confirmed by numerous experimental studies and quantum-mechanical computations [3,53,57].

The EDD in skatole (Fig. 5) shows that the excitation to the ^1L_a state leads to a shift of the electron density from the pyrrole ring, and an opposite CT process would take place in the case of fluorescence. In contrast, the EDD of ^1L_b is complicated and involves a stronger ED redistribution but within a smaller part of the molecule. The methyl group in indole introduces a more complicated localization pattern for both states, but dominated by CT from the pyrrole end, and in particular from the *N* atom. The dipole moment of the ^1L_a excited state is oriented approximately through the pyrrole *N* atom, making an angle with the ^1L_b dipole moment $\angle\mu_{La}\mu_{Lb}$ of 65° in skatole (Fig. 5a) whereas the same angle in indole is 102° (Fig 5b). This is in good agreement

with experiment, where the transition dipoles for these states are nearly perpendicular to each other, and where the dipole transition moment of the ^1L_b state is much smaller than for ^1L_a [57].

Another useful tool for identifying a chromophore is to compare EDDs for the same states in different structural models. For all compounds investigated, the coordinates of the indole units were the same. Skatole is the smallest adequate model of the chromophore, reproducing the main spectral features of the Trp residue in biological polymers. The ED distributions in indole, skatole, and Trp2Ala were compared in their relaxed ground electronic states as well as in both of the spectroscopically active ^1L_a and ^1L_b excited states. EDD_{GS} for all these molecules in their ground states (Fig. 6) were obtained by subtracting the ED of the larger structure from that of the smaller one, i.e. ED_{trp} or ED_{skt} from ED_{ind} and ED_{trp} from ED_{skt}. The excited-state EDD_{La} or EDD_{Lb} for each pair are presented without their corresponding EDD_{GS} to clearly show the difference between these states. For clarity, hydrogen atoms are not shown in Fig. 6, and in all cases, only the C_β atom are included, thus not showing the methyl group or the two alanine residues. Even though the ED_{GS} differ only in the bond with the C_β atom, we observe significant ED redistribution in the excited states of indole when compared to skatole and Trp2Ala. In contrast, the EDD between Trp2Ala and skatole is insignificant for both states. Thus, skatole reproduces more correctly the spectral features of Trp than a simple indole model due to the presence of the methyl group at the 3-position, mimicking the effect of alanyl and other residues. Thus, skatole is the appropriate chromophore for the Trp residue, in agreement with an earlier study [3].

The spectroscopic properties of indole and its methyl-substituted forms have been extensively studied both experimentally and theoretically, as it is the most spectroscopically active region of biological molecules. However, there are only a few studies in which the optimized excited-state structures and excitation energies of the ^1L_a and ^1L_b states in indole and skatole have been calculated using accurate *ab initio* methods. One of these studies have used the CASPT2/CASSCF/ANO-S (C,N[4s3p1d]/H[2s]) approach, which is often found to work well for small molecules [16,58]: with a level shift of 0.30 Hartree, the level-shifted CASPT2 approach has been shown to give excellent agreement with measured data for indole, ^1L_a=262 nm (f=0.08) and ^1L_b=280 nm (f=0.05), to be compared with experimental observations of ^1L_a=260 nm (f=0.11) and ^1L_b=284 nm (f=0.05), respectively.

An alternative approach that has been successfully used to calculate the spectral properties is the semi-empirical ZINDO approach [3,18,34,59]. Zerner's spectroscopically calibrated semi-empirical INDO-CIS approach, which is designed to correctly reproduce low-lying excited states, has been successfully used for a series of combined MD and QM studies [3,34]. However, there have been no reports of successful TDDFT investigations, and we here aim to close this gap.

The good agreement between the CASPT2/ANO results and the experimental data allows us to consider this method as a benchmark for studying other structures based on the indole core. However, the method is very expensive and cannot be used to calculate the hundreds or even thousands of conformers needed to generate even a single statistically averaged absorption or emission spectrum. In contrast, in the parameterized INDO-CIS method, hundreds of calculations can be carried out rather quickly, but it requires that the method is calibrated against the results of high-level *ab-initio* calculations.

The existence of two nearly isoenergetic, low-lying excited singlet states is a complicating factor, which gets further complicated by the fact that either of them can be the lowest state depending on the environment, as discussed above. The weakest ^1L_b state has normally the lowest excitation energy for structures derived from indole. This trend is reproduced by almost all computational methods for indole itself. However, at the CMB/aug level of theory, the ^1L_a and ^1L_b energy ordering are consistently reversed when a substituent is attached to the third C_γ site of indole, as it leads to a reduction in the excitation energy of ^1L_a, making this the lowest state even though the indole backbone remains the same (Table 2), in disagreement with both experimental and theoretical data [3,17]. Published structural parameters obtained with different electronic-structure methods are collected in Table 2.

For all structures reported in Table 2, which in addition to literature values include structures optimized at the CAM/aug level of theory and structures obtained from a scaling procedure to reach

inversion of these states with minimum changes in the bond lengths, we have calculated the excitation energies of the ^1L_a and ^1L_b states using both CMB/aug and QOP. For comparison, these states were also calculated using CAM-B3LYP with the ANO-RCC basis set [60,61] and the aug-cc-pVDZ basis set in the EOM-CCSD approach [62]. The values of the excitation energies and the oscillator strengths do not depend strongly on whether the aug-cc-pVDZ or ANO-RCC basis sets are used, but there is a significant difference in the computational time between these two basis sets, with ANO-RCC being the significantly more computationally expensive.

The excited states obtained with these different structures are all acceptable, but all TDDFT calculations exhibit the same weakness in that the lowest state is the ^1L_a state, and the excitation energies are overestimated by up to 20 nm. Several hybrid and long-range corrected functionals were tested using various basis sets all giving the same incorrect ordering of the excited states but with insignificant shifts of a couple of nm. In contrast, EOM-CCSD provides the correct ordering of these states, though also in this case the absorption bands are overestimated by about 20 nm. We would expect CASPT2 or EOMCCD with the aug-cc-pVDZ and ANO-RCC basis sets to be of similar quality, but the EOM-CCSD results are notably higher than the experimental and benchmark results of the excited states [17].

In practical calculations involving a large number of conformations, as is the case in the statistical SQMMD approach, a compromise must be made between accuracy and computational cost. None of the TDDFT approaches we explored were able to give excitation energies in good agreement with experiment, in all cases overestimating the excitation energies, however, the correct energy ordering of the states could be recovered. When exploring the dependence of the excitation energies on the changes in the pyrrole bonds, the excitation energies changes only moderately, but the ordering of the ^1L_a and ^1L_b states changes when increasing the N_1-C_2 bond distance, decreasing the C_2-C_3 bond length, and also to some extent the N_1-C_8 bond of the scaled structure (Fig.1, Table 2). This explains the reversal of the energy ordering of the states when a methyl group is attached, because the MOs on pyrrole involving the attached fragment also has orbital contributions from the C_2-C_3 bond (Fig. 7). Changing the C-C bonds in the benzene ring does not significantly shift the excited states, i.e. a change in the bond length of 0.01Å gives an energy lowering of about 3-4 nm.

Comparing the semi-empirical QOP-CIS approach to TDDFT, QOP-CIS is found to be less sensitive to geometry changes due to the calibration of individual integrals and it also give results in good agreement with available data (Table 2). Both QOP-CIS and ZINDO-CIS are parametrized to give good excitation energies for the lowest excited states of organic compounds, and in particular the ^1L_a and ^1L_b states of indole and skatole. Using the CMB/aug optimized structures for skatole gives QOP-CIS calculated excitation energies of ^1L_a(λ=265nm; f=0.18) and ^1L_b(λ=291nm; f=0.02) (Table 2 and Fig. 8). In Fig. 8, we report the weights of the CIS configurations, and the MOs are plotted using isolines = 0.040 e^-/bohr^3. The corresponding intramolecular CT is illustrated by plotting the isosurface of squared MOs Differences (sqMOD) with a threshold of 0.004 e^-/bohr^3 in each point of the surface, as EDDs could for technical reasons not be obtained for these systems. The difference between the total electronic densities of states may differ significantly from that obtained from sqMOD, but the main features are reproduced, as can be seen from a comparison of these methods (Fig. 7 and 9). EDD gives more detailed information because it takes the entire ground or excited electron distribution into account, whereas sqMOD is less accurate since it only invokes MOs involved in the formation of molecular configuration for the truncated CIS wave function, omitting small contributions. Both methods give a qualitative picture of the changes in the electron density.

Using the same geometry, the excitation energies calculated at the CMB/aug level of theory are respectively ^1L_a(λ=257nm; f=0.08) and ^1L_b(λ=249nm; f=0.04) (Table 2 and Fig. 9), and give qualitatively similar MOs. Whereas ^1L_a changes by less than 10 nm compared to the QOP results, ^1L_b changes by 55 nm. This is due to a difference of the EDD on the C_2-$C_{3\gamma}$ bond. Based on the discussion above and the results in Table 2, we see that only the semiempirical INDO-CIS can be used to calculate the lowest

excited states of skatole at the ground-state geometry to generate absorption spectra with an acceptable accuracy.

2.1.2 Emission structures

The dependence of the Trp fluorescence on the polarity of the environment makes the modeling of the spectral profile for the emission spectrum difficult. This is further complicated by the presence of transitions overlapping with the ^1L_a state showing a stronger solvent sensitivity than the ^1L_b state and which produce not only mono-exponential emission, but also bi-, or even many-, folded fluorescence. The ^1L_a emission shifts to longer wavelengths in polar solvent [18] due to the involvement of the active polar nitrogen atom in the pyrrole ring. Kasha's rule defines fluorescence to occur from the lowest excited state, and the ^1L_b state is therefore suggested to dictate the fluorescence spectrum in vacuum, dilute gases and completely non-polar environments, whereas the most common fluorescence state is ^1L_a in the more commonly encountered polar environments, such as water and biologic objects [1,3,18]. The observed complicated emission decay has been proposed to be due to fluorescence from various rotamers of tryptophan rather than a simultaneous emissions from the two excited states [1,2], in accordance with Kasha's rule. Due to the proximity of the two lowest $\pi\pi^*$ excited states fluorescence can be occurred from both of the ^1L_a and ^1L_b states, as the ordering of the states may differ for individual conformers of tryptophan. The structure of the chromophore in both excited states, their photophysics, and a scheme for studying the excited-state energy decay have to be established before we can investigate more closely the CT arising from an intermolecular electron transition from Trp to a non-bonded ligand.

As both excited states can be expected to be involved in the emission depending on the given conformer, in particular rotamer, we consider the geometry of both of these states, optimized for each excited state and reported in Table 3. Even very small changes in bond angles and lengths, the largest shift in bond length being less than 0.08Å, lead to significant spectral shifts and a reversal of the ordering of the ^1L_b and ^1L_a states (Table 2 and 3). The electron distribution in the ground state and the ^1L_b state are similar, but very different in the ^1L_a state. The largest changes in the excited-state geometry of the ^1L_a compared to the optimized ground-state geometry occurs in the pyrrole ring at the N_1-C_2-C_3 end, where at the CMB/aug level of theory, N_1-C_2 becomes significantly shorter and C_2-C_3 has the largest bond-length increase of all bonds, –0.05Å and +0.08Å, respectively. The benzene ring also is deformed by stretching along the short molecular axis, but this does not significantly affect the spectral shifts. At the optimized geometry of the ^1L_a state, the calculated emission wavelength is very close to experiment. CT occurs in the opposite direction of that seen for the absorption process in the emission process (Figures 5, 7-9). The EDD in Fig. 10 is calculated as extracting the initial fluorescent state S_1, which is the ^1L_a state, from the ground state S_0. The calculated CIS for the emission is marked by an asterisk superscript and is expressed by a back-arrow associated with the transfer of an excited electron to the "parent" occupied MO. For ^1L_a(295nm;f=0.12)* it is found to be $0.95|\text{HOMO}\leftarrow\text{L+1}\rangle^*$. The pyrrole nitrogen atom actively participates in the CT, making the molecule sensitive to its microenvironment as discussed previously.

The TDDFT calculations reproduce the ^1L_a energy levels quite accurately, but overestimate ^1L_b by about 20-30 nm [63]. A series of TDDFT calculations of the ^1L_a excited-state structures using different functionals, from the simpler PBE0 through long-range corrected functionals as well as CAM-B3LYP, in combination with different basis sets such as SVP, def2TZVP, 6–311++g(d,p), aug-cc-pVDZ and ANO-RCC gave only very minor changes in the calculated fluorescence wavelengths, the differences not exceeding a few nm for either state allowing us to focus on only one of these methods. The CMB/aug calculated fluorescence of the ^1L_a state with λ=300 nm and f=0.11 is in very good agreement with the CASPT2/ANO benchmark values of λ=295 nm and the same oscillator strength (Table 3). This suggests that TDDFT can be used for the calculation of the fluorescence of different conformers extracted from a MD trajectory.

As noted, the ^1L_a emission is the most probable in water and amino acid sequences, whereas the ^1L_b transition was proposed to contribute to the complicated fluorescence profiles observed [1,2]. Both states calculated at the ^1L_b excited-state structure are significantly overestimated compared to absorption wavelengths. At the ^1L_b excited-state geometry, the two excited states, i.e. $^1L_a(266\text{nm};0.12)^*=0.82|\text{HOMO}\leftarrow\text{L+1}\rangle^*$ and $^1L_b(263\text{nm};0.12)^*= 0.61|\text{H}-1\leftarrow\text{L+1}\rangle^*\&0.22|\text{HOMO}\leftarrow\text{L+7}\rangle$, are found to be almost degenerate and this could explain the complicated emission manifolds in vacuum or neutral media. However, we will in the following focus on Trp in the presence of either amino acid sequences or water, where ^1L_a fluorescence is preferable.

Despite the perfect agreement of the TDDFT calculations with the experimental data for the ^1L_a fluorescence, we will nevertheless use the QOP-CIS approach as it gives a balanced description of both absorption and emission photo-processes, and gives in general rates of internal conversion that more accurately reflects the excited-state energy dissipation. The rate of internal conversion k_{ic} between close-lying states of the same ππ* type is in the range of 10^{12} s^{-1} to 10^{14} s^{-1} and are thus several orders of magnitude larger than the rate of fluorescence k_r, which is about 10^8 s^{-1}, making emission from the higher ^1L_b energy level impossible. As the QOP-CIS states of skatole are almost degenerate, the approach can correctly account for the fact that fluorescence may occur from both states all depending on the conformers occurring in the trajectory of the fluctuating molecule. Secondly, the agreement between the excitation energies calculated for skatole optimized in the ^1L_a fluorescence state with experiment allows the topological parts of the FF to be scaled a little for the MD simulation.

2.2 SQMMD spectra

2.2.1 Dynamic models.

The long wavelength bands of the absorption and emission spectra of HSA are fully determined by the Trp214 chromophore, which in turn is very sensitive to the chemical and structural features of its microenvironment. The absorption and fluorescence regions can be found at wavelengths of 240-280 nm and 307-370 nm, respectively. Moreover, as discussed in the previous sections, the ordering of the close-lying ^1L_b and ^1L_a energy levels depend on the polarity of the surrounding media, and this delicate balance will define the intensity profile of the observed spectra. Ligands trapped in subdomain IIA of drug site I of HSA near the Trp214 can cause a quenching of the fluorescence due to electron excitations from the Trp chromophore to the ligands. Depending on the types of electronic transitions, CT can occur when the tryptophan donor and a trapped acceptor molecule are separated by less than 8 nm [64,65], that requires partial overlaps of donor fluorescence with absorption bands between donor and acceptor and that the electronic transition between them are allowed by the selection rules. The types of transitions from Trp214 to the ligand are defined by possible wave functions, describing either the interactions between the excited states, the degree of overlap of the states and even mixing their MOs arising π-π stacking. This spectral tenability of these CT properties is a unique tool for studying the photochemical process and migration of ligands in biological systems.

In the case of the Dmz ligand, the long wavelength absorption band was reported to fully overlap with the fluorescence band of tryptophan [19]. In the MD simulations, the Dmz ligand trapped by HSA is moving within the subdomain IIA, but never very away from the Trp214 chromophore fragment and close enough to provide MO overlap and allow for π-π stacking of the ligand with the chromophore (Fig 11).

Both absorption and fluorescence spectra of the isolated molecules and the donor-acceptor complex were generated using all conformers extracted from the MD simulations of the dynamically fluctuating system. The total MD simulation time of 5 ns to sample the conformational space provided 1000 snapshots. The extracted snapshots were used directly without structural relaxation in QM calculations of their spectral properties. This simulation period is much longer than the time needed for a molecular vibration cycle (responsible for internal conversions), which is of the order of $10^{10}s^{-1}\div10^{14}s^{-1}$ and

comparable to the rate of absorption $10^8 s^{-1}$. These time-scales also makes it possible for us to not discuss in detail how the MD trajectory covers the total excited-state relaxation.

The average distance between the center of mass of the donor and the acceptor $\langle r_{cm} \rangle$ is 5.4 Å and varies from 4.3 Å to 6.9 Å. The smallest interatomic separations $\langle r_{min} \rangle$ are 2.5Å, and varies between 1.9Å and 3.9 Å (Fig. 11a). The conformers of the Trp214-Dmz complex are all restricted to the HSA pocket and are stabilized by a hydrogen bond between the oxygen atom of the nitro group in Dmz and the methyl group of Trp214, at the same time as there is steric repulsion between the methyl groups of the fragments compounds (Fig. 11b). The stability of the complex is strengthened by strong Van-der-Waals interactions between the two fragments and π-π-stacking, preventing the acceptor from leaving the donor unless an external force is applied. The short Van-der-Waals distances are close to the interatomic distances observed in covalent bonds, providing the necessary intermolecular interactions to allow for the CT excitations that would lead to fluorescence quenching.

2.2.2 Types of charge transfers

In contrast to previously reported processes in which intramolecular electron excitations are accompanied with CT arising from the fluorescent indole state to a lower excited state localized on attached amide groups [1,3], we here consider intermolecular CT to a non-bonded molecule trapped at the same HSA pocket and which gives rise to additional effects compared to the case of covalently bonded fragments.

A Dmz molecule is embedded into the subdomain IIA of HSA where Trp214 resides. This cavity is quite large and has sufficient space to allow us to neglect the electric field of the microenvironment in the QM calculation. These effects will be considered in future work. The majority of the 1000 structures of the complexes extracted from the MD trajectory are close to the parallel-displaced type, with different degree of MO overlap and π-π stacking. The NO_2 group has a significant influence on the formation of the two excited Dmz states that are lower in energy than the fluorescent ^1L_a state. As a consequence, these states are sensitive to the proximity of the indole ring due to the formation of hydrogen bonds with the nitro group that contributes significantly to the interaction between these molecules (Figures 12 and 13).

Several representative conformers of the Skt&Dmz complex were extracted from the MD trajectory performed on subdomain IIA of HSA in order to study different types of CT between the skatole donor and the ligand acceptors. One of these conformers were chosen because it had the smallest interatomic separations and thus the largest overlap of the MOs between the acceptor and the donor, leading to a large stabilization of the π-π stacking.

There are no standard force field parameters for MD simulations of molecular electronic excited states. Rather, molecules are assumed to be in their structurally relaxed electronic ground states. We have constructed an artificial skatole molecule from the optimal stretching and bending parameters of the OPLS-AA force field. CAM-B3LYP calculations of this molecule using the aug-cc-pVDZ and ANO-RCC basis sets give the same excitation wavelengths and oscillator strengths of $\lambda(^1L_a)$ = 267 nm, f = 0.09 and $\lambda(^1L_b)$ = 252 nm, f = 0.03. PBE0/svp gave rather similar results: $\lambda(^1L_a)$ = 270 nm, f = 0.07 and $\lambda(^1L_b)$ = 249 nm, f = 0.01. On contrast, QOP-CIS gives a more realistic description of the absorption structure, where the most intense level $\lambda(^1L_a)$ = 272 nm, f = 0.20 is almost the same as that of the DFT calculations, whereas the other state is changed dramatically, now being the lowest excited state, with $\lambda(^1L_b)$ = 294 nm, f = 0.02. As discussed previously, none of the ground-state structures gives results at the TDDFT level that are correct compared to experiment, and even though the scaled structure (see Table 2) reversed the ordering of the states into the correct ordering, their energies are far from correct. It thus appears that the statistical absorption spectra can currently only be generated using the semiemiprical INDO-CIS approach in order to get qualitative and quantitative agreement with experimental observations.

Fluorescence quenching is determined by the CT from the excited state of the skatole donor to the Dmz acceptor, and this requires a different set of stretching and bending parameters for the ^1L_a excited skatole structure and the ground-state Dmz absorption structure. We focus on the ^1L_a state as this corresponds to the dominating fluorescent state for biologic media in water. The CT process is significant for this donor-acceptor pair as these fragments are always very close to each in the HSA pocket (see the discussion in the previous section), and their emission and absorption spectra almost fully overlap. In order to be able analyze the CT probability, we need a way to describe the excited states involved and to compare different ways of excited-state energy relaxation. For this purposed, we have selected three conformers that are representative examples of different structures (a) an "ordinary" sample that involves neither of the two other cases, namely (b) coinciding states and (c) strong π-π stacking. (Table 4 and Fig. 13).

As noted previously, since the fluorescent ^1L_a excited states of these small individual molecules calculated at the CMB/aug level of theory give results in good agreement with experiment, this approach could be used to investigate the CT processes. However, DFT functionals still struggle with the description of CT excitations, and even more so for non-bonded complexes with large intermolecular separations [29,66], often yielding too long wavelengths. The INDO/sp-CIS approach implemented in the QOP block provides not only the correct wavelengths for the lowest excited states, but also allows the rates of electron transitions to be calculated, and this approach was therefore used in the following.

The isolated skatole has a strong fluorescence with k_r about 10^{08} s^{-1} that is quenched in the complex with Dmz by CT to this acceptor. This CT process can be interpreted as an internal conversion k_{ic} calculated in the "super-molecule" approach [10,67] and ranges from 10^{10} s^{-1} to 10^{12} s^{-1} depending on the conformer. The wavelengths of the excitations in the isolated molecules are closely related to the corresponding values in the corresponding complexes, though with some notable exceptions that are due to interactions between MOs in the two fragments that can be expressed in terms of the CIS expansions in the paired and isolated molecules. The CIS wave functions are presented for the three molecular configurations in Table 4, giving the largest configurations with a weight of more than 0.1 (squared coefficients) with a few important exceptions, using the notation described in Section 2.1.2. Emission or intermolecular CT from the ^1L_a state to a lower-energy state of the acceptor is accompanied by energy relaxation from higher- to lower-energy singly occupied MOs. These MOs are related to the parent doubly occupied and vacant MOs which formed the corresponding configuration |OMO→UMO⟩.

The *a*-conformer is the most common. In this case, the distance between the donor and the acceptor is so long that there are only weak MO interactions, but nevertheless short enough to assume some contribution of π-π stacking. The excited states of the individual molecules are shifted slightly in the complex, though the lowest excited state in Dmz and its corresponding oscillator strength is hardly changed. The probability of internal conversion through CT is significantly larger than the emission process, leaving less than 1% for fluorescence (Table 4). The MOs forming the corresponding states are primarily localized on the fragments (Fig 13a), but close-lying states also include contributions from the neighboring molecule. For example, the Dmz state λ=332 nm has a small "intermolecular configuration" of 0.05|HOMO→LUMO⟩, where the HOMO is primarily localized on skatole.

In the *b*-conformer, there is an accidental degeneracy of the excited-state energies of the different fragments, giving rise to a much stronger rate of internal conversion due to the small energy gap and the admixture of the configuration 0.07|HOMO→L+2⟩, which is localized on skatole, in the Dmz-excited state with λ=325 nm (Table 4 and Fig 13b). A similar picture is seen for the rare instances when the Dmz acceptor state is lowest in energy and almost coincides with the ^1L_a state, also giving rise to fluorescence in this complex (the *d*-conformer). The donor and acceptors are non-bonded parts of a super-molecule, but if they are close enough to each to other, then the MOs distributed on one fragment can interact with the neighboring fragment through "mixed configurations" involving different fragments or even an "intermolecular configuration" in which the MOs are delocalized over both fragments.

Both types of electronic exchange between the fragments are found in the *c*-conformers, where is strong π-π stacking due to the short distance between the π-electrons of the different fragments. When the separation becomes as short as 4.0-3.5Å, there is substantial delocalization between the two fragments and a significant shift in the energy levels. In this case, another "virtual" state with a wavelength of λ=363 nm also appears, arising from the "intermolecular configuration" 0.57|HOMO→LUMO⟩ (Table 4) obtained by exciting an electron from the occupied orbital of skatole to the virtual Dmz orbital. This state is unique to the complex and cannot be observed in the isolated molecules (Fig, 13c). The CIS wave-function of the ^1L_a λ=323 nm state contains a substantial contribution of the Dmz configuration 0.14|H-2←LUMO⟩, whereas the state λ=330 nm, to which the CT is transferred to, includes both types of electronic mixing, such as the skatole configuration 0.15|HOMO→L+2⟩ and "intermolecular configuration" 0.12|HOMO→LUMO⟩. Thus, the complex with strong MOs interactions exhibits all three types of energy exchange between the non-bonded donor and the acceptor, that is, intermolecular "interstate CT", and electron redistribution in both fragments in the form of "intrastate interconfigurational CT" and finally "intrastate intermolecular configuration CT". In all cases, there is a very low probability of skatole fluorescence in the presence of Dmz in the HSA pocket.

2.2.3 Generating absorbance, fluorescence, and charge transfer spectra

There are two different ways optical spectra of a dynamically fluctuating molecule experiencing the forces produced in a MD simulation can be calculated. One is a time-resolved approach in which the "temporal" spectral response is obtained directly from the MD fluctuating chromophore fragment [1,3]. The second approach is a bandwidth resolution technique where the "band" of the statistically generated spectrum is obtained as implemented in the SQMMD approach [10,11]. In this latter approach, we assume that we can convert the time propagation into an instantaneous ensemble with a low concentration of uncorrelated active spectral regions parts, in line with the ergodic hypothesis. The "temporal" method can be used to describe the spectral properties of individual molecules selected by a focused laser beam, whereas the "band" method allows the photophysics of numerous identical molecules in a broad focal spot to be investigated in an efficient manner.

MD runs were carried out with the optimal stretching and bending parameters for the indole ring scaled to the CMB/aug optimized bond lengths and angles of both the absorptive and fluorescent geometries (Tables 2, 3). All spectra where normalized so that the largest absorption band in all the conformers was set to one.

As discussed earlier, TDDFT is unable to correctly reproduce the absorption bands in the long wavelength region, whereas the lowest excited state of the ^1L_a optimized structure (Table 3) has an excitation wavelength in perfect agreement with the calculated and measured fluorescence in the gas phase of 295 nm [58]. In contrast, the semi-empirical QOP-CIS provides acceptable results for both photophysical processes, allowing both absorption and fluorescence spectra to be modeled, including both the ^1L_b and ^1L_a transitions (see Fig. 14). The weak ^1L_b transition contributes to the absorption intensity and to the quantum yield of fluorescence if this state is the lowest for a given conformer, but the strong ^1L_a transition which almost fully overlaps with the ^1L_b band, defines the spectral shapes of both processes. The ^1L_a transition dipole moment μ_i is directed from "the center of the electronic charge" to the *N* atom of the pyrrole ring (see Fig. 14) and defines the main polarization of fluorescence through the oscillator strength f_i, which can be expressed as $f_i = 2/3K(E_2 - E_1)\ \mu_i^2$ where the energies E are in cm^{-1} and the coefficient $K=m_e/\hbar^2$ is given in SI units [68]. This information is very useful if a polarized emission can be observed in external fields or induced by nonlinear many-photon pumping, such as degenerate or non-degenerate two-photon absorption [69].

Ideally, the fluorescence spectra should be generated from averaged unitless quantum yields $\gamma = k_r/(k_r+\Sigma k_{st})$ for each energy bin, where k_{st} is the cross-section transition from the lowest singlet state to one or more triplet levels [10,70] rather than the plain emission rate However, as the CT from the donor to the acceptor through internal conversion in the super-molecule system are more than four orders of

magnitude more likely than the integrated transition to the triplet sub-system, we will here only consider the plain emission process as the decay through intersystem crossings will be negligible for the overall emission process.

Since TDDFT using CMB/aug works well for the isolated Dmz in the ground state and for the ^1L_a excited-state structure of tryptophan, the corresponding fluorescence spectra were calculated using the same conformers in order to compare with the QOP-CIS results. Both the "band" and "temporal" spectra were calculated (see Fig. 15 for a comparison). We note that the CMB/aug calculated ^1L_a and ^1L_b transitions overlap to a lesser extent and are more easily separated than in the QOP calculation. Nevertheless, also in this case the intense ^1L_a state defines the fluorescence band. There are only very few conformers for which ^1L_b can emit on the blue (shorter) side of the long-wavelength band, but this nevertheless does not change the dominant ^1L_a contribution (Fig. 15a). For the majority of the conformers, the ^1L_a fluorescence dominates because the internal conversion from the higher-lying ^1L_b level is 2-4 orders of magnitude faster than the emission from the ^1L_a state (see Tables 4). We observe the two typical fluorescent peaks for indole, though the ^1L_b band contributes almost nothing to fluorescence (Fig. 15b). The fluorescent profile arises from the fluctuation of the molecules, producing groups of conformations, and in particular rotamers, that are responsible for the inhomogeneous intensity distribution in the long wavelength spectral region. This fluorescence spectrum overlaps completely with the Dmz absorption band, as is necessary for an efficient CT process.

Earlier studies have reported different angles between the ^1L_a and ^1L_b dipole transition moments depending on their structures and the level of computation, though in all cases suggesting an angle close to 90°. The individual conformers exhibit a wide range for this angle, ranging from 11° to 170° (see Fig. 15c) whereas the angles between the oscillator strengths range from 2° to 90° (Fig. 15d) along the MD trajectory. The average values for the relative orientation are 90° and 76°, respectively, in good agreement with experiment. Since it is not possible to assign a unique wavelength for both states simultaneously for the different angles, the wavelength of the most intense fluorescent ^1L_a state was used in the figures.

We used the QOP-CIS results to overlap the tryptophan fluorescence spectrum with the Dmz absorption band as these are the most accurate for both states and they are needed to calculate the rates of deactivations in order to identify the excited-state energy degradation process. A single Trp214 residue in the original HSA backbone in the absence of a ligand exhibits a sharper fluorescence profile than that obtained for the excited states of the isolated skatole as extracted from the skatole-Dmz MD trajectory (Fig. 16a). The efficient CT from the donor to the acceptor is made possible by the overlap of the skatole fluorescence profile with the Dmz absorption band, in agreement with experimental data [19].

The theoretical spectra are narrower than the experimental spectra. There are several reasons for this, such as limitations in the MD simulation due to the approximate treatment the vibrational modes, the neglect of nonadiabatic transitions, and the approximate description of the charge distribution in the microenvironment in the QM calculation. The strong rate of internal conversion from the skatole ^1L_a state to the closest lower-lying Dmz singlet state arises from the close contact between the donor and acceptor moieties, allowing for a high degree of mixing of the MOs localized on the two fragments (Fig. 16b).
The probability of radiationless decay is several orders of magnitude higher than the emission from skatole, making the fluorescence quenching of Trp almost 100% in the presence of Dmz.

5. Conclusion

Different methods for calculating the lowest excited states of tryptophan and the corresponding electron density redistribution for the absorption and emission transitions to and from the ^1L_a and ^1L_b excited states have been presented. Three different kinds of intermolecular charge transfer processes from the tryptophan donor to the dimetrodiazole acceptor in the HSA cavity have been identified: 1) from the excited state of Trp to the lower excited singlet states formed from MOs fully localized on either of the two ligands, which we can denote as "interstate CT", 2) through electron redistribution within the same state where one or more molecular configurations of the CIS wave function are formed, allowing electron

transfer between the two molecules through an "intrastate intermolecular configuration CT", and 3) using "intrastate interconfigurational CT" where the CIS wave function is a linear combination of molecular configurations of the two non-bonded fragments.

The MD simulations showed that there could be strong MO interactions between the π-electrons of the dimetrodiazole ligand and the Trp214 residue inside HSA at the subdomain IIA of the binding site I, and that the separation between the centers of mass of the units is on average about 5.4 Å, but never exceeds 6.9 Å, and that the separation of the closest-lying atoms of these non-bonded molecules is on average about 2.5 Å, but never exceeds 3.9 Å without applying an external force. This allows for strong MO interactions between the molecules which together with a complete overlap of the emission band of the donor and absorption band of the acceptor provide the dominant mechanism for intermolecular CT to the embedded ligand, explaining the observed spectral shift and fluorescence quenching of Trp in the presence of ligands. The probability of radiationless decay is several orders of magnitude larger than the emission from tryptophan, giving rise to an extremely efficient fluorescence quenching in the presence of dimetrodiazole.

Acknowledgements

This work was supported by the Tomsk State University Academic D. I. Mendeleev Fund Program (Project No. 8.1.08.2015). This work has received support from the Norwegian Supercomputer Programme NOTUR through a grant of computer time (Grant No NN4654K). KR has been supported by the Research Council of Norway through a Centre of Excellence Grant (Grant No 179568).

References

[1] F.R. Beierlein, O.G. Othersen, H. Lanig, S. Schneider, T. Clark, Simulating FRET from Tryptophan: Is the Rotamer Model Correct?, J. Am. Chem. Soc. 128 (2006) 5142–5152. doi:10.1021/ja058414l.

[2] J.R. Lakowicz, Principles of fluorescence spectroscopy, 3rd ed, Springer, New York, 2006.

[3] P.R. Callis, Simulating electrostatic effects on electronic transitions in proteins, Mol. Simul. 41 (2015) 190–204. doi:10.1080/08927022.2014.923571.

[4] F. Melaccio, N. Ferré, M. Olivucci, Quantum chemical modeling of rhodopsin mutants displaying switchable colors, Phys. Chem. Chem. Phys. 14 (2012) 12485–12495. doi:10.1039/C2CP40940B.

[5] M.M. Huntress, S. Gozem, K.R. Malley, A.E. Jailaubekov, C. Vasileiou, M. Vengris, J.H. Geiger, B. Borhan, I. Schapiro, D.S. Larsen, M. Olivucci, Toward an Understanding of the Retinal Chromophore in Rhodopsin Mimics, J. Phys. Chem. B. 117 (2013) 10053–10070. doi:10.1021/jp305935t.

[6] C. Bernini, T. Andruniów, M. Olivucci, R. Pogni, R. Basosi, A. Sinicropi, Effects of the Protein Environment on the Spectral Properties of Tryptophan Radicals in Pseudomonas aeruginosa Azurin, J. Am. Chem. Soc. 135 (2013) 4822–4833. doi:10.1021/ja400464n.

[7] P.S. Chelushkin, D.V. Krupenya, Y.-J. Tseng, T.-Y. Kuo, P.-T. Chou, I.O. Koshevoy, S.V. Burov, S.P. Tunik, Water-soluble noncovalent adducts of the heterometallic copper subgroup complexes and human serum albumin with remarkable luminescent properties, Chem Commun. 50 (2014) 849–851. doi:10.1039/C3CC48008A.

[8] J.T. Vivian, P.R. Callis, Mechanisms of tryptophan fluorescence shifts in proteins., Biophys. J. 80 (2001) 2093–2109.

[9] C.-P. Pan, P.L. Muiño, M.D. Barkley, P.R. Callis, Correlation of Tryptophan Fluorescence Spectral Shifts and Lifetimes Arising Directly from Heterogeneous Environment, J. Phys. Chem. B. 115 (2011) 3245–3253. doi:10.1021/jp111925w.

[10] V. Pomogaev, A. Pomogaeva, P. Avramov, K.J. Jalkanen, S. Kachin, Thermo-dynamical contours of electronic-vibrational spectra simulated using the statistical quantum–mechanical methods, Theor. Chem. Acc. 130 (2011) 609–632. doi:10.1007/s00214-011-0936-6.

[11] V.A. Pomogaev, V.Y. Artyukhov, Theoretical Investigation of the Optical Spectra of Organic Compounds in Natural Surrounding, Russ. Phys. J. 59 (2016) 525–535. doi:10.1007/s11182-016-0802-z.

[12] D. Li, M. Zhu, C. Xu, J. Chen, B. Ji, The effect of Cu2+ or Fe3+ on the noncovalent binding of rutin with bovine serum albumin by spectroscopic analysis, Spectrochim. Acta. A. Mol. Biomol. Spectrosc. 78 (2011) 74–79. doi:10.1016/j.saa.2010.08.069.
[13] K.A. Majorek, P.J. Porebski, A. Dayal, M.D. Zimmerman, K. Jablonska, A.J. Stewart, M. Chruszcz, W. Minor, Structural and immunologic characterization of bovine, horse, and rabbit serum albumins, Mol. Immunol. 52 (2012) 174–182. doi:10.1016/j.molimm.2012.05.011.
[14] F. Samari, B. Hemmateenejad, M. Shamsipur, M. Rashidi, H. Samouei, Affinity of Two Novel Five-Coordinated Anticancer Pt(II) Complexes to Human and Bovine Serum Albumins: A Spectroscopic Approach, Inorg. Chem. 51 (2012) 3454–3464. doi:10.1021/ic202141g.
[15] S. Gorinstein, I. Goshev, S. Moncheva, M. Zemser, M. Weisz, A. Caspi, I. Libman, H.T. Lerner, S. Trakhtenberg, O. Martín-Belloso, Intrinsic tryptophan fluorescence of human serum proteins and related conformational changes, J. Protein Chem. 19 (2000) 637–642.
[16] L. Serrano-Andrés, B.O. Roos, Theoretical Study of the Absorption and Emission Spectra of Indole in the Gas Phase and in a Solvent, J. Am. Chem. Soc. 118 (1996) 185–195. doi:10.1021/ja952035i.
[17] A.C. Borin, L. Serrano-Andrés, A theoretical study of the absorption spectra of indole and its analogs: indene, benzimidazole, and 7-azaindole, Chem. Phys. 262 (2000) 253–265. doi:10.1016/S0301-0104(00)00336-0.
[18] P.L. Muiño, P.R. Callis, Hybrid simulations of solvation effects on electronic spectra: Indoles in water, J. Chem. Phys. 100 (1994) 4093. doi:10.1063/1.466347.
[19] W. Zhang, F. Wang, X. Xiong, Y. Ge, Y. Liu, SPECTROSCOPIC AND MOLECULAR DOCKING STUDIES ON THE INTERACTION OF DIMETRIDAZOLE WITH HUMAN SERUM ALBUMIN, J. Chil. Chem. Soc. 58 (2013) 1717–1721. doi:10.4067/S0717-97072013000200016.
[20] H. Xu, N. Yao, H. Xu, T. Wang, G. Li, Z. Li, Characterization of the Interaction between Eupatorin and Bovine Serum Albumin by Spectroscopic and Molecular Modeling Methods, Int. J. Mol. Sci. 14 (2013) 14185–14203. doi:10.3390/ijms140714185.
[21] K.W. Short, P.R. Callis, Evidence of pure 1Lb fluorescence from redshifted indole-polar solvent complexes in a supersonic jet, J. Chem. Phys. 108 (1998) 10189–10196. doi:10.1063/1.476478.
[22] V. Pomogaev, F.L. Gu, A. Pomogaeva, Y. Aoki, Elongation Method for Calculating Excited States of Aromatic Molecules Embedded in Polymers, Int. J. Quantum Chem. 109 (2009) 1328–1340. doi:10.1002/qua.21965.
[23] N.A. Borisevich, T.F. Raichenok, Absorption, fluorescence, and fluorescence excitation spectra of free molecules of indole and its derivatives, J. Appl. Spectrosc. 74 (2007) 245–250. doi:10.1007/s10812-007-0038-3.
[24] A. Sułkowska, Interaction of drugs with bovine and human serum albumin, J. Mol. Struct. 614 (2002) 227–232. doi:10.1016/S0022-2860(02)00256-9.
[25] Y. Wang, B. Tang, H. Zhang, Q. Zhou, G. Zhang, Studies on the interaction between imidacloprid and human serum albumin: spectroscopic approach, J. Photochem. Photobiol. B. 94 (2009) 183–190. doi:10.1016/j.jphotobiol.2008.11.013.
[26] Gaussian 09 Citation, (n.d.). http://www.gaussian.com/g_tech/g_ur/m_citation.htm.
[27] T.H. Dunning, Gaussian basis sets for use in correlated molecular calculations. I. The atoms boron through neon and hydrogen, J. Chem. Phys. 90 (1989) 1007. doi:10.1063/1.456153.
[28] T. Yanai, D.P. Tew, N.C. Handy, A new hybrid exchange–correlation functional using the Coulomb-attenuating method (CAM-B3LYP), Chem. Phys. Lett. 393 (2004) 51–57. doi:10.1016/j.cplett.2004.06.011.
[29] M.J.G. Peach, P. Benfield, T. Helgaker, D.J. Tozer, Excitation energies in density functional theory: An evaluation and a diagnostic test, J. Chem. Phys. 128 (2008) 044118. doi:10.1063/1.2831900.
[30] M.J.G. Peach, C.R.L. Sueur, K. Ruud, M. Guillaume, D.J. Tozer, TDDFT diagnostic testing and functional assessment for triazene chromophores, Phys. Chem. Chem. Phys. 11 (2009) 4465. doi:10.1039/b822941d.
[31] Dalton/LSDalton, (n.d.). http://daltonprogram.org/ (accessed April 25, 2016).
[32] K. Aidas, C. Angeli, K.L. Bak, V. Bakken, R. Bast, L. Boman, O. Christiansen, R. Cimiraglia, S. Coriani, P. Dahle, E.K. Dalskov, U. Ekström, T. Enevoldsen, J.J. Eriksen, P. Ettenhuber, B. Fernández, L. Ferrighi, H. Fliegl, L. Frediani, K. Hald, A. Halkier, C. Hättig, H. Heiberg, T. Helgaker, A.C. Hennum, H. Hettema, E. Hjertenaes, S. Høst, I.-M. Høyvik, M.F. Iozzi, B. Jansík, H.J.A. Jensen, D. Jonsson, P.

Jørgensen, J. Kauczor, S. Kirpekar, T. Kjaergaard, W. Klopper, S. Knecht, R. Kobayashi, H. Koch, J. Kongsted, A. Krapp, K. Kristensen, A. Ligabue, O.B. Lutnaes, J.I. Melo, K.V. Mikkelsen, R.H. Myhre, C. Neiss, C.B. Nielsen, P. Norman, J. Olsen, J.M.H. Olsen, A. Osted, M.J. Packer, F. Pawlowski, T.B. Pedersen, P.F. Provasi, S. Reine, Z. Rinkevicius, T.A. Ruden, K. Ruud, V.V. Rybkin, P. Sałek, C.C.M. Samson, A.S. de Merás, T. Saue, S.P.A. Sauer, B. Schimmelpfennig, K. Sneskov, A.H. Steindal, K.O. Sylvester-Hvid, P.R. Taylor, A.M. Teale, E.I. Tellgren, D.P. Tew, A.J. Thorvaldsen, L. Thøgersen, O. Vahtras, M.A. Watson, D.J.D. Wilson, M. Ziolkowski, H. Ågren, The Dalton quantum chemistry program system: The Dalton program, Wiley Interdiscip. Rev. Comput. Mol. Sci. 4 (2014) 269–284. doi:10.1002/wcms.1172.

[33] C. Adamo, V. Barone, Toward reliable density functional methods without adjustable parameters: The PBE0 model, J. Chem. Phys. 110 (1999) 6158. doi:10.1063/1.478522.

[34] P.R. Callis, Predicting fluorescence lifetimes and spectra of biopolymers, Methods Enzymol. 487 (2011) 1–38. doi:10.1016/B978-0-12-381270-4.00001-9.

[35] M.C. Zerner, Semiempirical Molecular Orbital Methods, in: K.B. Lipkowitz, D.B. Boyd (Eds.), Rev. Comput. Chem., John Wiley & Sons, Inc., Hoboken, NJ, USA, 1991: pp. 313–365. http://doi.wiley.com/10.1002/9780470125793.ch8 (accessed April 25, 2016).

[36] V. Pomogaev, A. Pomogaeva, Y. Aoki, Absorption Spectra of Estradiol and Tryptophan Constructed by the Statistical and Elongation Methods, J. Phys. Chem. A. 113 (2009) 1429–1433. doi:10.1021/jp808262h.

[37] V.Y. Artyukhov, A.I. Galeeva, Spectroscopic parametrization of the method of PNDO, Sov. Phys. J. 29 (1986) 949–952. doi:10.1007/BF00898453.

[38] G.V. Maier, V.Y. Artyukhov, N.R. Rib, Nature of the electron-excited states and the mechanism of nonradiative energy transfer in aromatic bifluorophores, Russ. Phys. J. 36 (1993) 949–954. doi:10.1007/BF00559159.

[39] V.G. Plotnikov, Regularities of the processes of radiationless conversion in polyatomic molecules, Int. J. Quantum Chem. 16 (1979) 527–541. doi:10.1002/qua.560160311.

[40] V.Y. Artyukhov, V.A. Pomogaev, Three-center integrals of one-electron operator of a spin-orbit interaction, Russ. Phys. J. 43 (2000) 590–600. doi:10.1007/BF02508964.

[41] V.A. Pomogaev, V.Y. Artyukhov, Spin-Orbital Interaction in Molecular Complexes of Naphthalene with Anthracene Derivatives, J. Appl. Spectrosc. 68 (2001) 251–258. doi:10.1023/A:1019264118932.

[42] I. Petitpas, A.A. Bhattacharya, S. Twine, M. East, S. Curry, Crystal Structure Analysis of Warfarin Binding to Human Serum Albumin ANATOMY OF DRUG SITE I, J. Biol. Chem. 276 (2001) 22804–22809. doi:10.1074/jbc.M100575200.

[43] rscb.org, (n.d.). http://ww2.rscb.org/?folio=9POSOZI1U (accessed December 26, 2016).

[44] http://www.gromacs.org/, (n.d.).

[45] W.L. Jorgensen, J. Chandrasekhar, J.D. Madura, R.W. Impey, M.L. Klein, Comparison of simple potential functions for simulating liquid water, J. Chem. Phys. 79 (1983) 926–935. doi:10.1063/1.445869.

[46] Tppmktop, (n.d.). http://erg.biophys.msu.ru/erg/tpp/ (accessed December 19, 2016).

[47] B. Hess, H. Bekker, H.J.C. Berendsen, J.G.E.M. Fraaije, LINCS: A linear constraint solver for molecular simulations, J. Comput. Chem. 18 (1997) 1463–1472. doi:10.1002/(SICI)1096-987X(199709)18:12<1463::AID-JCC4>3.0.CO;2-H.

[48] R.S. Mulliken, Electronic Population Analysis on LCAO–MO Molecular Wave Functions. I, J. Chem. Phys. 23 (1955) 1833–1840. doi:10.1063/1.1740588.

[49] F.L. Hirshfeld, Bonded-atom fragments for describing molecular charge densities, Theor. Chim. Acta. 44 (1977) 129–138. doi:10.1007/BF00549096.

[50] J.P. Foster, F. Weinhold, Natural hybrid orbitals, J. Am. Chem. Soc. 102 (1980) 7211–7218. doi:10.1021/ja00544a007.

[51] U.C. Singh, P.A. Kollman, An approach to computing electrostatic charges for molecules, J. Comput. Chem. 5 (1984) 129–145. doi:10.1002/jcc.540050204.

[52] M.T.P. Beerepoot, A.H. Steindal, N.H. List, J. Kongsted, J.M.H. Olsen, Averaged Solvent Embedding Potential Parameters for Multiscale Modeling of Molecular Properties, J. Chem. Theory Comput. 12 (2016) 1684–1695. doi:10.1021/acs.jctc.5b01000.

[53] J.N. Scott, P.R. Callis, Insensitivity of Tryptophan Fluorescence to Local Charge Mutations, J. Phys. Chem. B. 117 (2013) 9598–9605. doi:10.1021/jp4041716.
[54] R.R. Valiev, V.N. Cherepanov, V.Y. Artyukhov, D. Sundholm, Computational studies of photophysical properties of porphin, tetraphenylporphyrin and tetrabenzoporphyrin, Phys. Chem. Chem. Phys. 14 (2012) 11508. doi:10.1039/c2cp40468k.
[55] A. Osted, J. Kongsted, K.V. Mikkelsen, P.-O. Åstrand, O. Christiansen, Statistical mechanically averaged molecular properties of liquid water calculated using the combined coupled cluster/molecular dynamics method, J. Chem. Phys. 124 (2006) 124503. doi:10.1063/1.2176615.
[56] Y. Mochizuki, Y. Komeiji, T. Ishikawa, T. Nakano, H. Yamataka, A fully quantum mechanical simulation study on the lowest n–π∗ state of hydrated formaldehyde, Chem. Phys. Lett. 437 (2007) 66–72. doi:10.1016/j.cplett.2007.02.016.
[57] N. Sharma, S.K. Jain, R.C. Rastogi, Solvatochromic study of excited state dipole moments of some biologically active indoles and tryptamines, Spectrochim. Acta. A. Mol. Biomol. Spectrosc. 66 (2007) 171–176. doi:10.1016/j.saa.2006.02.039.
[58] S. Pistolesi, A. Sinicropi, R. Pogni, R. Basosi, N. Ferré, M. Olivucci, Modeling the Fluorescence of Protein-Embedded Tryptophans with ab Initio Multiconfigurational Quantum Chemistry: The Limiting Cases of Parvalbumin and Monellin, J. Phys. Chem. B. 113 (2009) 16082–16090. doi:10.1021/jp9080993.
[59] L.S. Slater, P.R. Callis, Molecular Orbital Theory of the 1La and 1Lb States of Indole. 2. An ab Initio Study, J. Phys. Chem. 99 (1995) 8572–8581. doi:10.1021/j100021a020.
[60] EMSL Basis Set Exchange, (n.d.). https://bse.pnl.gov/bse/portal (accessed December 16, 2016).
[61] B.O. Roos, R. Lindh, P.-\AAke Malmqvist, V. Veryazov, P.-O. Widmark, Main group atoms and dimers studied with a new relativistic ANO basis set, J. Phys. Chem. A. 108 (2004) 2851–2858. doi:10.1021/jp031064.
[62] M. Kállay, J. Gauss, Calculation of excited-state properties using general coupled-cluster and configuration-interaction models, J. Chem. Phys. 121 (2004) 9257. doi:10.1063/1.1805494.
[63] S. Grimme, E.I. Izgorodina, Calculation of 0–0 excitation energies of organic molecules by CIS(D) quantum chemical methods, Chem. Phys. 305 (2004) 223–230. doi:10.1016/j.chemphys.2004.06.050.
[64] D. Li, J. Zhu, J. Jin, X. Yao, Studies on the binding of nevadensin to human serum albumin by molecular spectroscopy and modeling, J. Mol. Struct. 846 (2007) 34–41. doi:10.1016/j.molstruc.2007.01.020.
[65] S. Speiser, Photophysics and mechanisms of intramolecular electronic energy transfer in bichromophoric molecular systems: solution and supersonic jet studies, Chem. Rev. 96 (1996) 1953–1976. doi:10.1021/cr941193+.
[66] V. Pomogaev, S.P. Tiwari, N. Rai, G.S. Goff, W. Runde, W.F. Schneider, E.J. Maginn, Development and application of effective pairwise potentials for UO2n+, NpO2n+, PuO2n+, and AmO2n+ (n = 1, 2) ions with water, Phys. Chem. Chem. Phys. 15 (2013) 15954. doi:10.1039/c3cp52444b.
[67] H. Haken, H.C. Wolf, Macromolecules, Biomolecules, and Supermolecules, in: Mol. Phys. Elem. Quantum Chem., Springer Berlin Heidelberg, Berlin, Heidelberg, 2004: pp. 473–501. http://link.springer.com/10.1007/978-3-662-08820-3_20.
[68] R.C. Hilborn, Einstein coefficients, cross sections, f values, dipole moments, and all that, Am. J. Phys. 50 (1982) 982. doi:10.1119/1.12937.
[69] S. Herbrich, T. Al-Hadhuri, K.-H. Gericke, P.S. Shternin, A.G. Smolin, O.S. Vasyutinskii, Two-color two-photon excited fluorescence of indole: Determination of wavelength-dependent molecular parameters, J. Chem. Phys. 142 (2015) 024310. doi:10.1063/1.4905140.
[70] V.A. Pomogaev, V.Y. Artyukhov, Quantum-chemical study of spectral-luminescent properties of indole, Atmospheric Ocean. Opt. 15 (2002) 213.

Fig.1 tryptophan

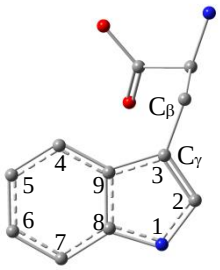

Fig.2 Ligand&Trp214@HSA

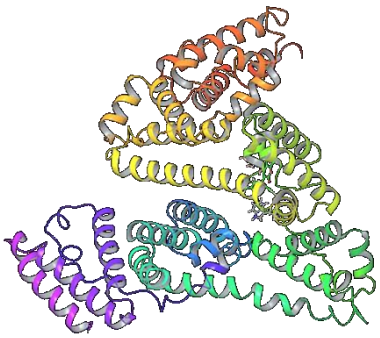

Fig.3 Dmz&Trp@HSA and system of local coordinates for the complex

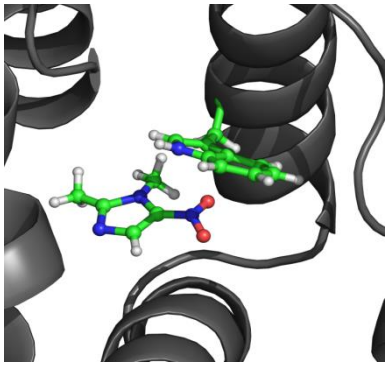

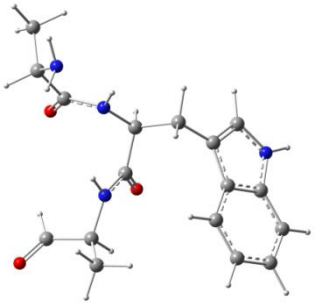

Fig.4 Trp with 2 Ala fragment of HSA

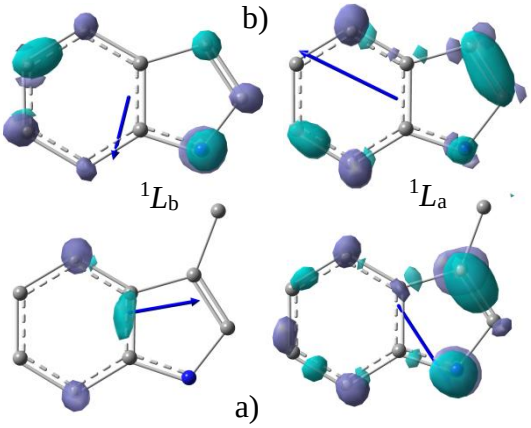

Fig. 5. The dark lilac space shows a positive EDD (increasing ED) between ground states and ^1L_a or ^1L_b of (a) skatole and (b) indole. The blue arrows denote dipole orientations.

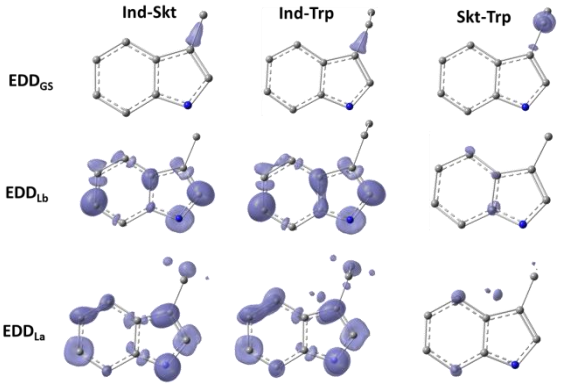

Fig. 6. Lilac space denotes a positive EDD between indole, skatole portions of tryptophan in GS, ^1L_a and ^1L_b states. 0.002 e^-/bohr^3

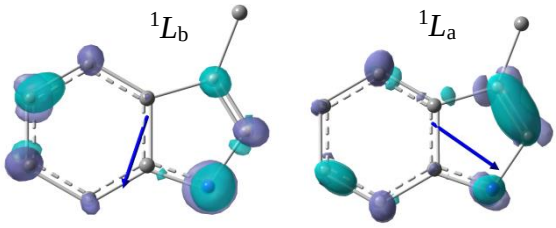

Fig. 7. The dark lilac space shows a positive EDD (increasing ED) between ground states and ^1L_a or ^1L_b of skatole and blue arrows denotes dipole orientations.

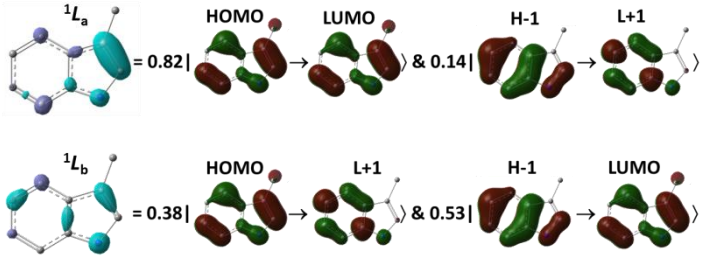

Fig. 8. The dark lilac space is increasing ED represented by sqMOD for ^1L_a or ^1L_b states of skatole calculated with QOP-CIS.

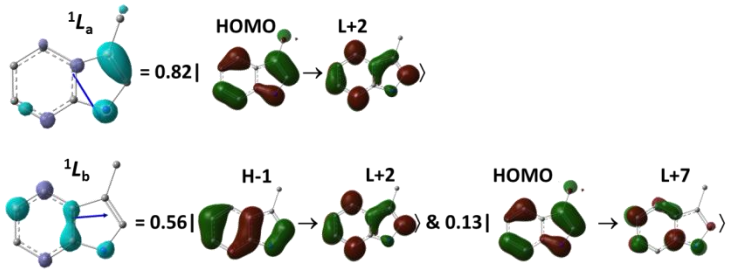

Fig. 9. The dark lilac space is increasing ED represented by sqMOD for ^1L_a or ^1L_b states of skatole calculated with CMB/aug.

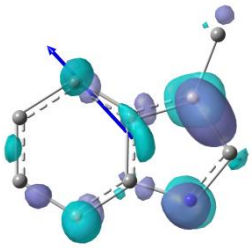

Fig. 10. EDD ($S_0 - S_1$) for emission of CMB/aug optimized skatole in ^1L_a

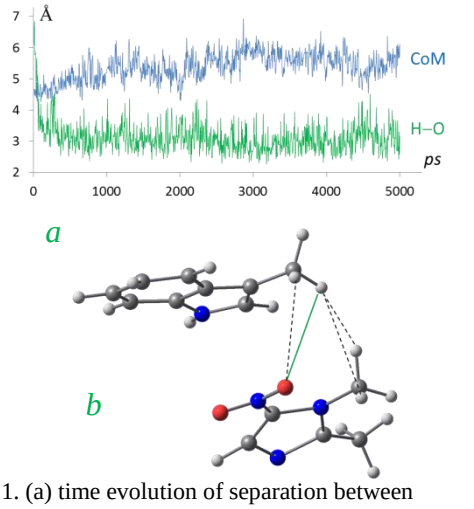

Fig. 11. (a) time evolution of separation between Trp214 and Dmz measured between their centers of mass (blue) and minimum H-bond to nitro group (green) and (b) a complex sketch with minimal spaces.

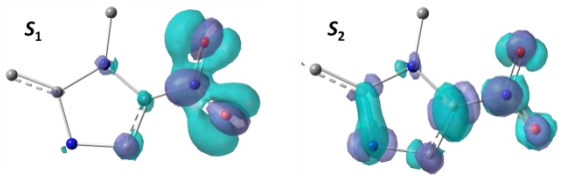

Fig. 12. EDD absorptions to the lowest excited states.

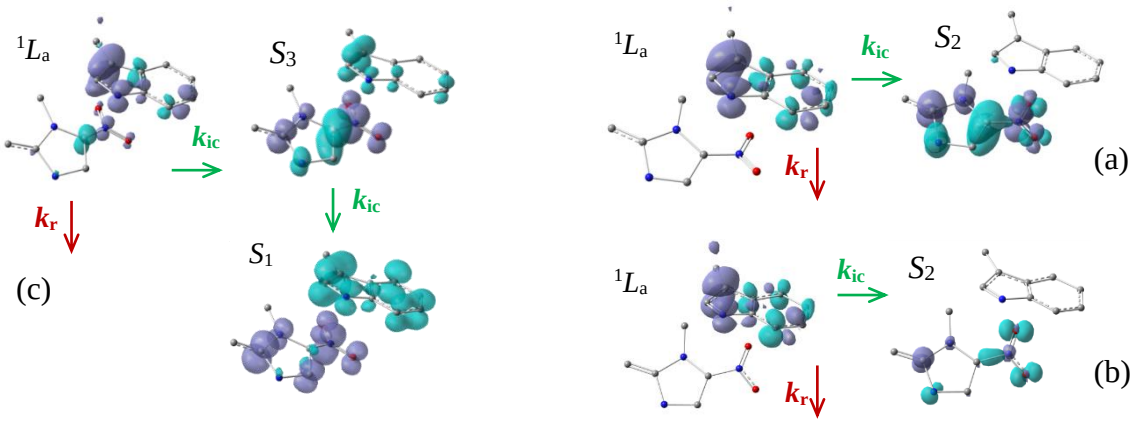

Fig.13. sqMOD plotting fluorescence quenching by means of CT from ^1L_a to Dmz (isolines = 0.002 e^-/bohr^3) for 3 typical ways, (a) ordinary sample, (b) coinciding states, (c) strong π-π stacking (Table 4)

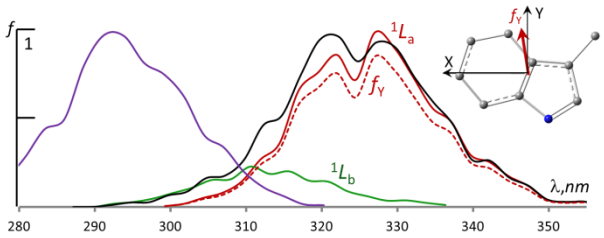

Figure 14. QOP calculated absorbance (violet) and fluorescence ^1L_b (green lower) and ^1L_a (red higher) bands with major polarization in molecular system of coordinates.

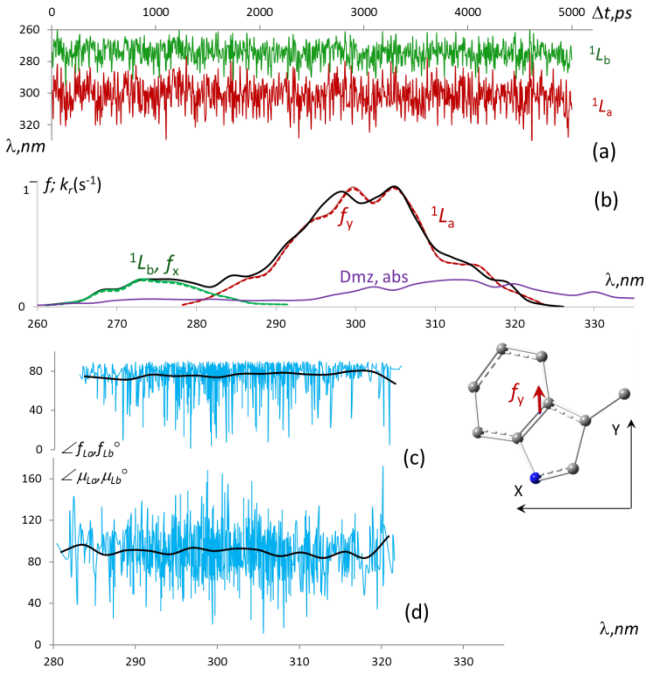

Fig. 15. CMB/aug calculated and generated ^1L_a and ^1L_b fluorescence spectra of a) "time resolution" bands and b) overlapping "bandwidth resolution" profiles and their main polarizations (dashed) with Dmz absorption. Distribution angles between dipole moments (c) and oscillator strengths (d) of these states along the fluctuation of ^1L_a wavelengths.

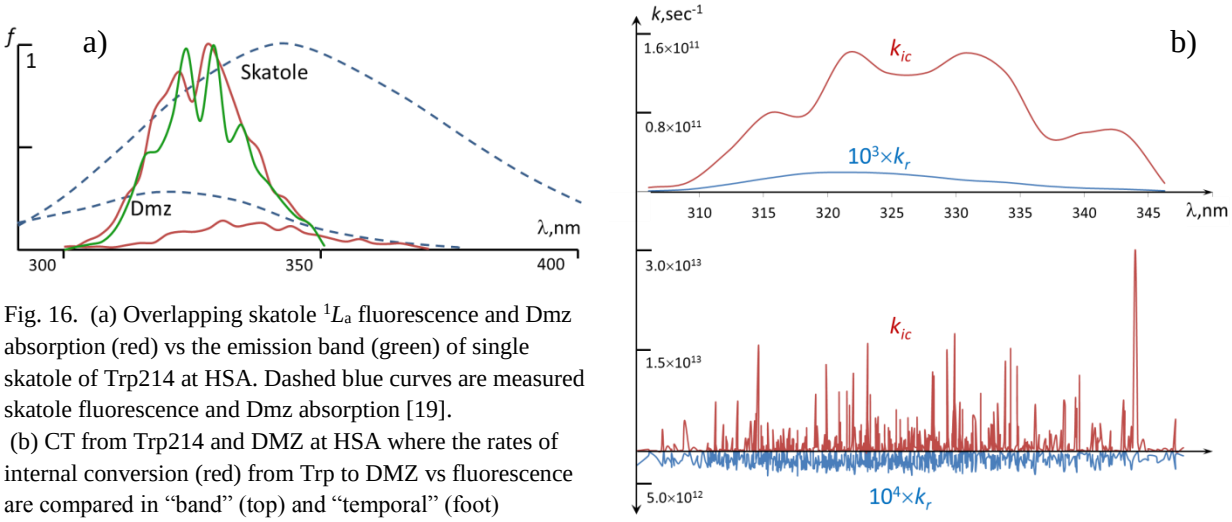

Fig. 16. (a) Overlapping skatole ^1L_a fluorescence and Dmz absorption (red) vs the emission band (green) of single skatole of Trp214 at HSA. Dashed blue curves are measured skatole fluorescence and Dmz absorption [19].
(b) CT from Trp214 and DMZ at HSA where the rates of internal conversion (red) from Trp to DMZ vs fluorescence are compared in "band" (top) and "temporal" (foot) representations.

Table 1. Low-lying excited states with wavelengths (λ,nm) and oscillator strengths (f)

states	Trp2Ala	tryptophan	3-alanyl-indole	skatole	indole
L_b	252(0.05)	251(0.05)	253(0.03)	249(0.04)	248(0.04)
L_a	256(0.09)	256(0.08)	258(0.08)	257(0.08)	**246(0.10)**

Table 2. Bonds optimized, taken from Ref [16,18,58,59], scaled for absorption structures of skatole (skt) and indole (ind) together with partial atomic charges (in parenthesis) used for MD as well as corresponding the low-lying excited ^1L_a and ^1L_b states with oscillator strengths (in parenthesis) calculated in different approaches (see details in footnote).

Bonds	indole CMB/aug (e^{-1})	$[58]_{skt}$	$[16]_{ind}$	$[18]_{skt}$	$[59]_{ind}$	scaled
N_1-C_2	1.382 (–0.158)	1.379	1.379	1.38	1.380	1.400
C_2-C_3	1.367 (+0.015)	1.364	1.369	1.34	1.376	1.296
C_3-C_9	1.443 (+0.103)	1.450	1.445	1.45	1.430	1.450
C_9-C_4	1.404 (+0.028)	1.408	1.410	1.41	1.423	1.410
C_4-C_5	1.385 (+0.024)	1.386	1.388	1.40	1.408	1.410
C_5-C_6	1.409 (–0.155)	1.412	1.417	1.39	1.388	1.410
C_6-C_7	1.385 (+0.090)	1.387	1.389	1.39	1.413	1.410
C_7-C_8	1.398 (–0.209)	1.402	1.405	1.40	1.389	1.410
C_8-C_1	1.375 (+0.361)	1.371	1.374	1.39	1.401	1.360
C_8-C_9	1.414	1.406	1.410	1.38	1.377	1.410

states	skatole	indole	skatole	Indole	skatole	indole	skatole	indole	skatole
$^{org}L_b$			277(0.02)	280(0.05)	290			224(0.21)	
$^{org}L_a$			249(0.09)	260(0.08)	270			219(0.05)	
$^{cba}L_b$	249(0.04)	248(0.04)	249(0.05)	249(0.04)	245(0.04)	250(0.06)	248(0.02)	246(0.03)	253(0.04)
$^{cba}L_a$	257(0.08)	246(0.10)	256(0.08)	247(0.10)	258(0.08)	242(0.06)	266(0.11)	259(0.12)	245(0.06)
$^{ano}L_b$	250(0.04)		249(0.05)						
$^{ano}L_a$	257(0.08)		256(0.07)						
$^{qop}L_b$	291(0.02)	289(0.02)	290(0.02)	289(0.02)	287(0.02)	285(0.02)	289(0.02)	287(0.01)	292(0.02)
$^{qop}L_a$	265(0.18)	263(0.17)	264(0.17)	257(0.17)	262(0.17)	260(0.16)	273(0.26)	271(0.26)	258(0.10)
$^{emc}L_b$	258(0.03)								
$^{emc}L_a$	244(0.09)								

(^{org}) labels the original data; (^{qop}) means semiempirical QOP-CIS; CAM-B3LYP applied with aug-cc-pVDZ (^{cba}) and ANO-RCC (^{ano}) basis sets; EOM-CCSD used with aug-cc-pVDZ (^{emc}) .

Table 3. Optimized bonds, taken from Ref [16,58], scaled for excited structures of skatole (skt) and indole (ind) together with partial atomic charges (in parenthesis) used for the MD simulations, as well as the corresponding the lowest fluorescence ^1L_a or ^1L_b bands with oscillator strengths (in parenthesis) calculated in different approaches (see details in footnote).

	optimized to L_a morphology					optimized to L_b morphology			
bonds	indole CMB/aug (e^{-1})		$[58]_{skt}$	$[16]_{ind}$	scaled	indole CMB/aug		$[58]_{skt}$	$[16]_{ind}$
N_1-C_2	1.343 (–0.133)		1.323	1.376	1.343	1.394		1.391	1.393
C_2-C_3	1.436 (+0.013)		1.446	1.472	1.437	1.388		1.381	1.384
C_3-C_9	1.423 (+0.122)		1.445	1.411	1.423	1.419		1.43	1.427
C_9-C_4	1.420 (–0.049)		1.415	1.471	1.420	1.417		1.417	1.419
C_4-C_5	1.420 (+0.024)		1.427	1.374	1.430	1.413		1.442	1.446
C_5-C_6	1.377 (–0.153)		1.376	1.430	1.380	1.428		1.439	1.441
C_6-C_7	1.448 (+0.092)		1.446	1.465	1.450	1.411		1.432	1.434
C_7-C_8	1.391 (–0.219)		1.395	1.386	1.390	1.413		1.41	1.412
C_8-C_1	1.401 (+0.335)		1.425	1.391	1.400	1.364		1.367	1.368
C_8-C_9	1.406		1.401	1.432	1.434	1.460		1.459	1.463
states	skatole	indole	skatole	indole	skatole	skatole	indole	skatole	indole
$^{org}L_a$			295(0.11)	291					
$^{cba}L_b$	272(0.01)	253(0.01)	256(0.00)		260(0.01)	262(0.06)	259(0.05)	270(0.06)	266(0.03)
$^{cba}L_a$	295(0.12)	278(0.14)	300(0.11)	284(0.22)	294(0.12)	266(0.09)	253(0.12)	264(0.07)	260(0.11)
$^{ano}L_b$			257(0.00)		260(0.01)			270(0.06)	
$^{ano}L_a$			300(0.11)		295(0.12)			264(0.07)	
$^{qop}L_b$	301(0.00)	299(0.03)	300(0.12)		306(0.00)	305(0.02)	304(0.03)	308(0.02)	307(0.02)
$^{qop}L_a$	299(0.30)	291(0.29)	303(0.18)	291(0.39)	299(0.31)	276(0.19)	274(0.17)	277(0.17)	269(0.16)
$^{emc}L_b$	267(0.01)				260(0.01)				
$^{emc}L_a$	277(0.12)								

(^{org}) labels the original data; (^{qop}) means semiempirical QOP-CIS; CAM-B3LYP applied with aug-cc-pVDZ (^{cba}) and ANO-RCC (^{ano}) basis sets; EOM-CCSD used with aug-cc-pVDZ (^{emc}) .

Table 4. The typical schemes of CT for fluorescence quenching illustrated with three types of conformers (Fig. 13). Each two columns successively present wavelengths in nm, oscillator strengths in parenthesis, and the rates of radiation and internal conversion (s^{-1}) vs CIS expansion (local numbering of MOs). Three pairs of columns are the complex and separated fragments.

Skt&DMZ	CIS	skatole	CIS	Dmz	CIS
a-conformer of ordinary sample					
349(0.06)	0.22|H-2→LUMO⟩ 0.38|H-5→LUMO⟩ 0.19|H-5→L+1⟩			348(0.06)	0.40|H-2→LUMO⟩ 0.20|HOMO→LUMO⟩ 0.19|H-2→L+1⟩
332(0.19)	0.58|H-2→LUMO⟩ 0.13|H-5→LUMO⟩ 0.05|HOMO→LUMO⟩			330(0.27)	0.71|HOMO→LUMO⟩ 0.11|H-2→LUMO⟩
316(0.25)^{La} k_r =1.7×10^{08}	0.75|HOMO←L+2⟩*	320(0.27)^{La} k_r =1.9×10^{08}	0.84|HOMO←LUMO⟩*		

k_{ic}=8.0×10^{10}					
b-conformer of coinciding states					
357(0.09)	0.39|H-2→LUMO⟩ 0.23|H-5→LUMO⟩ 0.18|H-5→L+1⟩			358(0.11)	0.40|HOMO→LUMO⟩ 0.23|H-2→LUMO⟩ 0.17|H-2→L+1⟩
325(0.12)	0.49|H-2→LUMO⟩ 0.16|H-5→LUMO⟩ 0.07|HOMO→L+2⟩			325(0.21)	0.54|HOMO→LUMO⟩ 0.17|H-2→LUMO⟩
320(0.34)^{La} k_r =2.4×10^{08} k_{ic}=2.5×10^{12}	0.79|HOMO←L+2⟩*	324(0.26)^{La} k_r =1.7×10^{08}	0.88|HOMO←LUMO⟩*		
c-conformer of strong π-π stacking					
363(0.13) ^{S1}	0.57|HOMO→LUMO⟩ 0.19|H-2→LUMO⟩				
359(0.01) ^{S2}	0.49|H-5→LUMO⟩ 0.17|HOMO→LUMO⟩ 0.14|H-5→L+1⟩			360(0.02)	0.56|H-2→LUMO⟩ 0.16|H-2→L+2⟩ 0.15|H-2→L+1⟩
330(0.03) ^{S3}	0.46|H-2→LUMO⟩ 0.12|HOMO→LUMO⟩ 0.15|HOMO→L+2⟩			334(0.34)	0.85|HOMO→LUMO⟩
323(0.34)^{La} k_r =2.3×10^{08} k_{ic}=2.1×10^{12}	0.43|HOMO←L+2⟩* 0.21|HOMO←L+5⟩* 0.14|H-2←LUMO⟩	326(0.23)^{La} k_r =1.4×10^{08}	0.66|HOMO←LUMO⟩* 0.18|HOMO←L+3⟩*		